The effect of foreground subtraction on cosmological measurements from intensity mapping

L. Wolz,[1,2]★ F. B. Abdalla,[1] C. Blake,[3] J. R. Shaw,[4] E. Chapman[1] and S. Rawlings[2]†

[1]*Department of Physics and Astronomy, University College London, London WC1E 6BT, UK*
[2]*Sub-Department of Astrophysics, Department of Physics, University of Oxford, The Denys Wilkinson Building, Keble Road, Oxford OX1 3RH, UK*
[3]*Centre for Astrophysics and Supercomputing, Swinburne University of Technology, PO Box 218, Hawthorn, VIC 3122, Australia*
[4]*Canadian Institute for Theoretical Astrophysics, 60 St. George Street, Toronto, ON M5S 3H8, Canada*

ABSTRACT

We model a 21-cm intensity mapping survey in the redshift range $0.01 < z < 1.5$ designed to simulate the skies as seen by future radio telescopes such as the Square Kilometre Array, including instrumental noise and Galactic foregrounds. In our pipeline, we remove the Galactic foregrounds with a fast independent component analysis technique. We present the power spectrum of the large-scale matter distribution, $C(\ell)$, before and after the application of this foreground removal method and calculate the systematic errors. Our simulations show a certain level of bias remains in the power spectrum at all scales $\ell < 400$. At large-scales $\ell < 30$ this bias is particularly significant. We measure the impact of these systematics in two ways: first we fit cosmological parameters to the broad-band shape of the $C(\ell)$ where we find that the best fit is significantly shifted at the 2–3σ level depending on masking and noise levels. However, secondly, we recover cosmic distances without biases at all simulated redshifts by fitting the baryon acoustic oscillations in the $C(\ell)$. We conclude that further advances in foreground removal are needed in order to recover unbiased information from the broad-band shape of the $C(\ell)$, however, intensity mapping experiments will be a powerful tool for mapping cosmic distances across a wide redshift range.

Key words: methods: statistical – cosmological parameters – large-scale structure of Universe – radio lines: galaxies.

1 INTRODUCTION

Cosmological parameters can be estimated via the measurement of the large-scale distribution of the galaxies. This has been successfully performed over the last decade with optical surveys (e.g. Percival et al. 2001; Tegmark et al. 2004, 2006; Blake et al. 2011; Thomas, Abdalla & Lahav 2011). The accuracy of parameter estimation is significantly increased if the survey covers a large fraction of the sky and can access high redshifts. However, this is challenging at optical wavelengths because integration times are usually long and the high resolution needed to get data from each individual galaxy makes the survey speed slow.

In most types of survey, the field-of-view (FoV) is a feature of the telescope design and not adjustable during the observations. The present and next generation of radio interferometers, such as Low Frequency Array (LOFAR)[1] (van Haarlem et al. 2013) and the Square Kilometre Array (SKA),[2] have been designed with new

technologies such as stations with phased array feeds as well as stations composed of dipoles. This means that surveys with flexible FoV and multibeaming can be easily arranged and performed within much shorter observing times. In this way the FoV of optical surveys, which is typically of the size of $\approx 1\,\mathrm{deg}^2$, can be greatly exceeded by future radio telescopes.

In the last decade, a technique called intensity mapping (see e.g. Ansari et al. 2008; Chang et al. 2008, 2010; Peterson et al. 2009; Vujanovic et al. 2009; Pritchard & Loeb 2012; Masui et al. 2013; Switzer et al. 2013) has been proposed. The basic idea is that the entire neutral hydrogen (H I) flux of a wide patch of the sky is measured in a coarse grid for each redshift bin. The generated maps of H I flux are then used to trace the mass content of every pixel. These maps are then used to constrain cosmological parameters through their power spectrum as in e.g. Abdalla & Rawlings (2005) and Abdalla, Blake & Rawlings (2010). The wide FoV together with a lack of resolution makes it relatively cheap and quick to observe a large fraction of the sky. Intensity mapping can naturally not recover very small-scale structure in the power spectrum, but with use of an appropriate FoV the baryon acoustic oscillations (BAO) imprinted in the matter distribution can be recovered, as shown in Wyithe, Loeb & Geil (2008).

★ E-mail: lwolz@star.ucl.ac.uk
† Deceased.
[1] http://www.lofar.org/
[2] http://www.skatelescope.org/

An important issue when dealing with intensity mapping data is the presence of strong Galactic foregrounds. Radio emission from the Milky Way has an intensity up to five orders of magnitude higher than the H I signal we are interested in. It is therefore of great importance to develop sophisticated foreground removal techniques which do not leave significant traces in the recovered signal. By analysing the cleaned maps we can measure to what degree the residuals of the Galactic foregrounds leftover in the data affect the cosmological fits. For example, the power spectrum of the matter density distribution can be distorted by foreground removal contamination, which can cause systematic errors in the cosmological analysis.

There have been extensive studies of the Galactic foregrounds and foreground removal (see e.g. Di Matteo et al. 2002; Oh & Mack 2003; Di Matteo, Ciardi & Miniati 2004; Santos, Cooray & Knox 2005; Morales, Bowman & Hewitt 2006; Wang et al. 2006; Gleser, Nusser & Benson 2008; Jelic et al. 2008; Harker et al. 2009; Liu et al. 2009; Bernardi et al. 2010; Liu & Tegmark 2011, 2012; Petrovic & Oh 2011; Chapman et al. 2012; Dillon, Liu & Tegmark 2013; Moore et al. 2013) for the epoch of reionization data as well as the cosmic microwave background (CMB). However, in the case of intensity mapping of the large-scale structure distribution at low redshifts, the field is relatively unexplored (Ansari et al. 2012). We investigate how well a more realistic simulation of the foregrounds can be cleaned with the fast independent component analysis (FASTICA) method developed by Hyvärinen (1999) for intensity mapping experiments with future radio telescopes.

In this work, we use an SKA-like simulation of the H I distribution and combine it with a Galactic foreground simulation in the redshift range 0.01–1.5. We remove the foregrounds with the FASTICA method and evaluate its performance as a function of sky masks and other settings related to the FASTICA technique. The power spectrum estimations from the resulting intensity maps are used to evaluate the effect of the foreground subtraction on the cosmological analysis, where we specifically investigate the bias in the cosmological parameters and the recovery of the BAO scale. The systematic errors in the foreground removal change the broad-band power of the cosmological signal, however, they do not introduce a preferred scale. This motivates that cosmic distances measurements, in this case the BAO scale, are more robust than the power spectrum measurement. In this way, we create an end-to-end simulation of a future intensity mapping experiment, from input noisy data cube to cosmological parameter fits.

The paper is structured as follows. Section 2 outlines the intensity mapping idea and reviews briefly the current state-of-the-art. We proceed with a detailed description of our simulation in Section 3. In Section 4, the power spectrum estimation of the intensity maps and the theoretical modelling of the power spectrum are presented. We briefly describe the independent component analysis (ICA) and its application to our data. The results of the foreground removed data are shown in Section 5. The cosmological parameter analysis and the resulting bias are presented in Section 6. We conclude in Section 7 with the discussion of the impact of our results for future intensity mapping surveys.

2 INTENSITY MAPPING

The basic concept of an intensity mapping survey is mapping the integrated line flux of a voxel rather than measuring every single galaxy with exact redshift information. The advantage is that a large sky coverage is feasible within a relatively short observing time at the expense of low resolution. In order to recover the BAO scale,

we chose the angle of the Gaussian beam which approximates the primary beam of the telescope, as $0°.3$. At the redshifts of interest for our study $z \approx 0.7$, the BAO scale subtends an angle of order of $3°$.

In principle, intensity mapping surveys are possible with every spectral line, for instance Lyman α in the optical (see Peterson & Suarez 2012; Pullen, Dore & Bock 2013) or the rotational CO lines with e.g. $\nu_{1-0} = 115\,\text{GHz}$ (e.g. Lidz et al. 2011; Visbal, Trac & Loeb 2011) in the radio frequency regime. However, the H I line with frequency $\nu = 1.42\,\text{GHz}$ is the commonly chosen line. Line confusion with different spectral line occurs if $\frac{\nu_1}{1+z_1} = \frac{\nu_2}{1+z_2}$, which often happens for different CO lines and also for Lyman α with other lines of the Lyman series. This kind of confusion is insignificant (Gong et al. 2011) for the 21-cm line because there is no other dominant spectral line close to its emitted frequency.

The ultimate intensity mapping experiment will be possible with the SKA, which is currently being planned. Also, there are SKA pathfinders, like ASKAP[3] and MeerKAT,[4] which may be able to undertake an intensity mapping survey within a shorter time-scale.

However, an H I intensity mapping survey can also be realized with a single, large ≈ 100 m dish, as shown with the Green Bank Telescope (GBT; Masui et al. 2013; Switzer et al. 2013). There are other single-dish radio telescopes proposed such as the BAOs in Neutral Gas Observations (BINGO) experiment (Battye et al. 2013). BINGO will observe the H I emission in redshifts range $0.13 < z < 0.48$ over $2000\,\text{deg}^2$ in 1 yr of observing time. A slightly different approach is chosen by the Canadian Hydrogen Intensity Mapping Experiment (CHIME)[5] design which uses cylindrical dishes as elements of an interferometer. The aim of the experiment is measuring the H I flux in a volume of $300\,\text{Gpc}^3$ covering the redshift range $0.8 < z < 2.5$. Another more recent planned project is the Tianlai[6] project (Chen 2012).

These planned surveys give very promising prospects for the future of intensity mapping. They will cover a very wide redshift range as well as large fraction of the observable sky.

3 SIMULATED DATA

In this section, we describe the data simulations used in this analysis. These simulations can be split in four components: the cosmological signal based on the SKA Design Study (SKADS) simulation (Wilman et al. 2008); the Galactic foreground (Shaw et al. 2014); the noise estimator and the lognormal realizations used for the computation of the covariances.

3.1 Wilman SKA simulation

The large-scale matter distribution used in this work is a semi-empirical simulation of the radio continuum sky up to redshift 20 as described in Wilman et al. (2008). A brief description of the properties of the simulation is given below. For a detailed description we refer the reader to Wilman et al. (2008).[7]

The simulation is based on a realization of the linear matter power spectrum produced by CAMB (Lewis, Challinor & Lasenby 2000). The cosmological model used in the Wilman SKA simulation is

---

[3] http://www.atnf.csiro.au/projects/mira/

[4] http://www.ska.ac.za/meerkat/

[5] http://chime.phas.ubc.ca/

[6] http://tianlai.bao.ac.cn/

[7] http://s-cubed.physics.ox.ac.uk/s3_sex

$\Omega_m = 0.3$, $\Omega_k = 0.0$, $w = -1.0$, $h = 0.7$, $f_{baryon} = 0.16$, $\sigma_8 = 0.74$, $b = 1.0$ and $f_{NL} = 0$. This density field realization is gridded in cells of size 5 Mpc h^{-1} from which galaxies are sampled. The galaxy bias function $b(z)$ follows the description of Mo & White (1996) with a cut-off redshift for different galaxy types. This cut-off is chosen so that the bias is held constant above a give redshift to prevent exponential blow-up of the clustering. Galaxy clusters are identified by looking for regions with overdensities larger than the critical density with use of the Press–Schechter (Press & Schechter 1974) and Sheth–Tormen formulations (Sheth & Tormen 1999). The simulation includes populations of four types of galaxies: radio-quiet active galaxy nuclei (AGN; Jarvis & Rawlings 2004), radio-loud AGN (Willott et al. 2001) of low and high luminosities and star-forming galaxies (Yun, Reddy & Condon 2001). The empirical luminosity functions of the different sorts of galaxies are extrapolated to high redshifts, since there are no relevant observations available in this regime so far. The H I masses of the galaxies are correlated with the star formation rate of galaxies (Wilman et al. 2008). They are assigned according to the correlation between the 1.4 GHz luminosity function given by Sullivan et al. (2001) and the H I masses (Doyle et al. 2005). This description is only valid for star-forming galaxies and, due to the lack of an irregular galaxy population in the simulation, the resulting H I mass function does not exactly match the locally observed mass function by Zwaan et al. (2003) in the redshift range $0 < z < 0.1$.

In this work, we made use of a half-sky extension of the publicly available $20° \times 20°$ simulation. This simulation is a half-sky realization of the same theoretical model as the original simulation, however, it has some limitations compared to the previously described one: it does not include AGN and clusters of galaxies and only extends to redshift 1.5. The initial cell size was also increased to 10 Mpc h^{-1}. For the purpose of our analysis, these changes are not significant, since intensity mapping uses coarse resolution and we want to examine the potential of future radio observations in a low-redshift regime. Also, we are most interested in the star-forming objects in this paper.

There are other, more accurate approaches to simulating galaxy distributions, such as hydrodynamical or semi-analytic methods. In this study, we examine intensity maps with half-sky coverage to high redshifts which cover a very large volume not currently available with other simulation approaches. In addition, the semi-empirical simulations are by construction tuned to reproduce the observational properties of the underlying galaxy distribution.

We constructed maps of the brightness temperature of the H I emission using these simulations. We converted the galaxy catalogue of the Wilman simulation into 21-cm brightness temperature maps following the description in Abdalla et al. (2010). Given the H I mass $M_{H I}$, the neutral hydrogen emissivity per steradian can be calculated using the emission coefficient of the 21-cm line transmissions A_{12}. We used the Rayleigh–Jeans law for low frequencies to convert the emissivity into the measurable brightness temperature per pixel:

$$T = \frac{3A_{12}hc^2}{32\pi m_H k} \frac{M_{H I}}{\chi^2(z)\Delta\nu\nu_{21}\Omega_{pix}}, \quad (1)$$

where h is the Planck constant, m_H is the mass of the hydrogen atom and k is the Boltzmann constant. In addition we use the comoving distance $\chi(z)$, width of the frequency slice $\Delta\nu$ and the solid angle of one resolution element Ω_{pix}. All the maps shown in this paper are in units of Kelvin.

Following the temperature conversion, the maps are smoothed to the resolution of the intensity mapping survey. We assume a
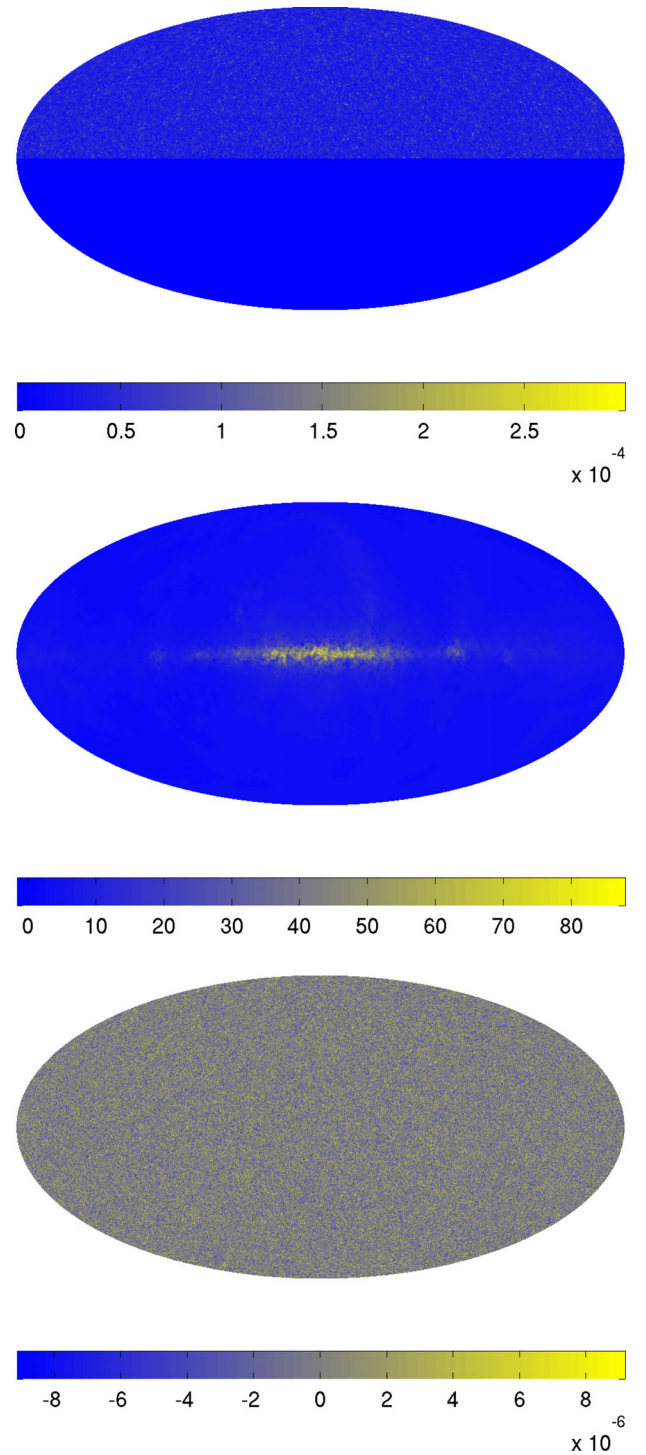
Figure 1. Simulated data (upper panel), Galactic foregrounds (middle panel) and noise maps (lower panel) for frequency $\nu = 829$ MHz with frequency width $\Delta\nu = 5.2$ MHz which corresponds to the redshift slice $0.71 < z < 0.72$. The colour bar represents brightness temperature in units of Kelvin.

Gaussian primary beam with a FoV constant in redshift. The solid angle of each resolution element is calculated via $\Omega = 1.33\theta_{FWHM}^2$, where θ_{FWHM} is the opening angle at the full width at half-maximum (FWHM) which is chosen as $0°.3$ throughout this study.

In Fig. 1 in the first panel, one example map of the Wilman simulation with frequency width $\Delta\nu = 5.2$ MHz is pictured. This

narrow binning width is used in the Galactic foreground removal in order to improve the performance. In the cosmological analysis wider binning is used so that the signal-to-noise ratio is increased in order to measure the BAOs and compress the data enough to obtain a reasonably sized data set.

3.2 Galactic foreground

The main contributions to the radio continuum emission of galaxies at the frequencies of interest are synchrotron and free–free electron emission (Condon 1992). The foregrounds produced by our Galaxy are well studied in the frequency range of the microwave background emission above 10 GHz. Our frequencies of interest ($570 < \nu < 1400\,\mathrm{MHz}$) are less explored and there are only two all-sky maps at $\nu = 408\,\mathrm{MHz}$ (the Haslam map by Haslam et al. 1982) and $\nu = 1420\,\mathrm{MHz}$ (Testori et al. 2001).

The foreground simulation used here is described in detail by Shaw et al. (2014). In this simulation the Haslam map is extrapolated with the help of a sky map of the radio spectral index, since observations have shown that the spectral index of the foreground is not constant with sky latitude. These maps of the spectral index are derived using the global sky model by de Oliveira-Costa et al. (2008). This method performs a principal component analysis (PCA) of the most relevant observations of the Milky Way in the radio regime and determines that the first three principal components are sufficient to create a global sky model of our galaxy. In addition, it takes the variation of the spectral index with latitude on the sky and frequency into account. We improve the resolution of our foreground maps, beyond that of the Haslam, by simulating small-scale variations. These are drawn from a multifrequency angular power spectrum constructed following the description in Santos et al. (2005). This uses power laws to model the angular fluctuations and frequency autocorrelations, but an exponential decorrelation between frequencies. Any large-scale variations in this realization, which are already included in the Haslam map, are removed and, to assure the smoothness of the total power spectrum, the variance on smaller scales than $5°$ is rescaled to the fluctuations of the Haslam map. This gives frequency structure beyond a pure power law, and adds in arbitrarily small angular structure, while remaining consistent with observational data. A Galactic foreground map of our simulations is shown in the second row of Fig. 1.

3.3 Lognormal realizations

In our analysis, we use the power spectrum of the large-scale structure in redshift shells to quantify the statistical properties of our simulated data set. To determine the covariance between data points in our simulated sky accurately, we require many mock realizations. Unfortunately, we only have one simulated SKA sky to analyse. We therefore built 100 lognormal realizations of the matter distribution from the same power spectrum used in the SKA simulation with the same redshift distribution of the H I-selected galaxies. We extracted their power spectra and cross-correlated them in order to estimate the covariance matrices of the power spectra of the simulated data between different angular scales and redshifts.

In order to compute the covariances in the power spectra of an intensity mapping observation, the lognormal realization need to be converted into temperature maps of the 21-cm flux. The H I masses of the galaxies of the lognormal simulations are assigned from the H I mass distribution according to the properties present in the SKA simulation. Specifically, we compute the cumulative histogram of the H I mass distribution in each redshift bin of the

simulation. We invert the cumulative histogram of the H I mass and fit a spline function to it. We draw a random number between 0 and 1 for each galaxy, multiply it by the total galaxy number and use the fitted spline function to draw the H I mass of each galaxy. With this procedure, the total H I density is preserved for each redshift bin. In the subsequent analysis, the lognormal galaxy catalogues are converted into smoothed temperature maps as described in Section 3.1.

3.4 Receiver noise

The receiver noise of a radio interferometer (Thompson, Moran & Swenson 2004; Abdalla et al. 2010) in the measured brightness temperature is given by

$$\Delta T_{\mathrm{b}} = \frac{c^2 T_{\mathrm{sys}}}{\nu^2 \Omega f A_{\mathrm{eff}} \sqrt{2 \Delta \nu t}}. \tag{2}$$

T_{sys} describes the system temperature of the radio receivers which has a goal of 10 K for the full SKA design, t is the integration time and A_{eff} is the effective collecting area of the telescope. It is convenient to combine the system temperature and the collecting area into one quantity since increasing the area has the same effect as decreasing the system temperature. The SKA design goal (Carilli & Rawlings 2004) is $A_{\mathrm{eff}}/T_{\mathrm{sys}} = 2.0 \times 10^4\,\mathrm{m^2\,K^{-1}}$. We are assuming a survey duration of 6 months, which in a case of a half-sky observation for our FoV results in an integration time per pointing of 77 s.

The parameter f describes what fraction of the full SKA configuration is being simulated. f ranges between 0 and 1. The rms of the brightness temperature scales as $1/\sqrt{N}$ with the number of pixel feeds N. We simulate the instrumental noise according to a 10 per cent SKA realization with $N = 25$ pixel feeds. However, f and N are completely degenerate, so this noise level would also describe a 50 per cent SKA observation with a single pixel feed. There are several other instrumental set-ups which can produce similar noise properties. For instance, single dishes rather than interferometers may be used to produce intensity mapping experiments. We do not discuss the advantages or disadvantages of such approaches in this paper.

As introduced in Section 3.1, $\Omega = 1.133\theta_{\mathrm{FWHM}}^2$ is the solid angle of our assumed Gaussian primary beam with opening angle θ_{FWHM}. We simulate a map of Gaussian noise smoothed to the width $\theta_{\mathrm{FWHM}} = 0°.3$. For the foreground removal, we chose a binning of the maps constant in frequency with bin width $\Delta \nu = 5.2\,\mathrm{MHz}$. A noise map according to the chosen frequency binning of the SKA simulation is pictured in Fig. 1 in the third row.

4 POWER SPECTRUM ESTIMATION

4.1 Data measurement

Assuming an observation in the redshift bin z_i, it is convenient to expand the matter distribution in spherical harmonic functions since we are observing the galaxy distribution on a sphere:

$$\sigma(\theta, \phi) = \sum_{\ell=0}^{\infty} \sum_{m=-\ell}^{\ell} a_{\ell m} Y_{\ell m}(\theta, \phi), \tag{3}$$

where σ is the surface density of galaxies at a given direction in the sky, with coefficients $a_{\ell m}$ and spherical harmonics $Y_{\ell m}(\theta, \phi) = \sqrt{\frac{(2\ell+1)(\ell-m)!}{4\pi(\ell+m)!}} P_\ell^m(\cos\theta) \mathrm{e}^{\mathrm{i}m\phi}$. Here P_ℓ^m denote the Legendre polynomials. The spherical harmonics are normalized such

that $\int Y_{\ell m}(\theta, \phi) Y^*_{\ell' m'}(\theta, \phi)\, d\Omega = \delta_{\ell\ell'}\delta_{mm'}$. Multiplying equation (3) by $Y^*_{\ell' m'}(\theta, \phi)$ and integrating over the solid angle Ω defines the back transformation:

$$a_{\ell m} = \int \sigma(\theta, \phi) Y^*_{\ell m}(\theta, \phi)\, d\Omega. \qquad (4)$$

The coefficients a_{lm} completely describe the properties of the galaxy distribution in spherical harmonic space. For an intensity mapping survey, the map consists of discrete temperature values T for every resolution element with solid angle $\Delta\Omega_{\text{pix}}$ rather than a continuous galaxy distribution σ. Hence, the integral in equation (4) becomes a summation over the pixels p_i of the map:

$$a^{\text{pix}}_{\ell m} = \sum_{i=1}^{N_{\text{pix}}} T(p_i) Y^*_{\ell m}(p_i) \Delta\Omega_{\text{pix}}. \qquad (5)$$

The power spectrum $C(\ell)$ is calculated via the autocorrelation of the spherical harmonic expansion. It contains information about the preferred correlation length of matter overdensities in the distribution. If the matter distribution is a realization of a Gaussian random field, the statistical properties of the distribution are completely described by the power spectrum and the mean of the expansion coefficients vanishes: $\langle a_{\ell m}\rangle = 0$. Then the variance is $\langle a_{\ell m} a^*_{\ell m}\rangle = C(\ell)$, which leads to the estimator of the power spectrum in spherical harmonic space:

$$C(\ell) = \frac{1}{2\ell + 1} \sum_{m=-\ell}^{\ell} |a_{\ell m}|^2. \qquad (6)$$

In most cases, there is no full sky observational data available. In terms of power spectrum estimation, this means that the estimator of equation (6) is biased, and measurements at different multipoles are correlated. In order to compare cut-sky observations to theoretical predicted full-sky power spectra, we need an unbiased power spectra for cut sky. In this work, we chose to account for the correlation and loss of power that the cut sky induces with the Peebles approximation (Peebles 1973). However, there are also other approaches to correct for this, most commonly the maximum likelihood approach (e.g. Efstathiou 2004):

$$C_{\text{Peebles}}(\ell) = \frac{1}{2\ell + 1} \sum_{m=-\ell}^{\ell} \frac{|a^{\text{gal}}_{\ell m} - \frac{N}{\Delta\Omega} I_{\ell m}|^2}{J_{\ell m}}, \qquad (7)$$

with

$$I_{\ell m} = \int_{\Delta\Omega} Y^*_{\ell m}(\theta, \phi)\, d\Omega; \quad J_{\ell m} = \int_{\Delta\Omega} |Y_{\ell m}(\theta, \phi)|^2\, d\Omega. \qquad (8)$$

Comparing $I_{\ell m}$ to equation (4), it represents the spherical harmonic coefficients of the mask, which has a value of 1 for areas within the observation and 0 elsewhere. For a full sky observation $I_{\ell m}$ should be 0 in all components. In addition, $J_{\ell m}$ weights the power spectrum according to the sky fraction such that it is 1 for complete sky. For a discrete analysis of intensity maps the integrals of equation (8) become sums over all pixels of the map.

4.2 Theoretical prediction

A theoretical prediction for the matter power spectrum $P(k, z)$ is obtained using a present day linear power spectrum estimate $P(k, z = 0)$ by CAMB (Lewis et al. 2000). The evolution of the power spectrum in time is estimated following linear perturbation theory

in the Newtonian description. The resulting differential equation for the growth factor reads

$$\ddot{D}(t) + \frac{2\dot{a}}{a}\dot{D}(t) = 4\pi G\bar{\rho}D(t). \qquad (9)$$

The resulting approximation for the time-dependent power spectrum is

$$P(k, z) = D^2(z)P(k, z = 0). \qquad (10)$$

The projected angular power spectrum $C(\ell)$ in linear theory can be calculated via Blake et al. (2004):

$$C(\ell) = \int P_0(k) W(\ell, k)\, dk, \qquad (11)$$

where $W(\ell, k)$ is a window function, which projects the power spectrum on to the sphere. For a more elaborate discussion see Huterer, Knox & Nichol (2001) and Tegmark, Hamilton & Xu (2002). Since our particular interest is not on the very large scales of the matter distribution, we use the small angle approximation for computational ease:

$$C(\ell) = b^2 \int P\left(k = \frac{\ell}{\chi(z)}, z\right) \chi^{-2}(z) p^2(z) \left(\frac{d\chi(z)}{dz}\right)^{-1} dz, \qquad (12)$$

which is valid for large l (Blake et al. 2004, 2007).

The bias function b reflects the fact that we observe the visible galaxy power spectrum, whereas the above derivations are valid for the matter distribution. Therefore we introduce the linear bias as $P_{\text{gal}}(k, z) = b^2(z)P(k, z)$. In the following, we will assume a redshift independence of the bias $b(z_i) = b$ within the redshift shell and marginalize over the unknown bias in the following analysis. The probability distribution of the galaxies $p(z)$ is set to constant within every redshift shell such that $p(z) = 1/\Delta z$ since the redshift shells are narrow. In this work, we neglect redshift space distortions since they only influence the large scales of the power spectrum and are not included in the Wilman simulation. In Fig. 2 the theoretical prediction of the $C(\ell)$ for redshift $0.61 < z < 0.67$ is pictured
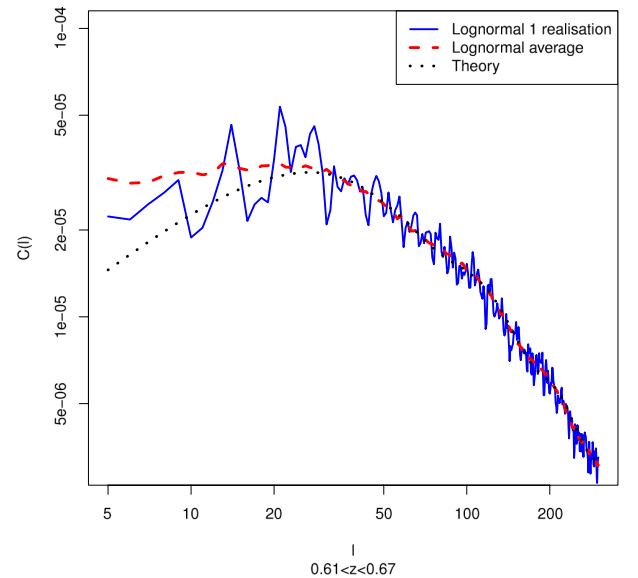
Figure 2. Theoretical prediction for the large-scale structure power spectrum (dotted black line) in comparison with estimated power spectrum of one lognormal realization (solid blue line) and the average of the estimated power spectrum of 100 lognormal realizations (dashed red line).

as the dotted black lines. The temperature power spectrum of one lognormal realization (blue line) and the average lognormal $C(\ell)$ (red line) are plotted. On large scales they mismatch the black line of the theoretically modelled power spectra due to the use of the small angle approximation, however, the agreement is good on scales $\ell > 20$. The graphs are shown with the shot noise removed.

4.3 Noise estimate

The noise present in the power spectrum measurement can be estimated as

$$\sigma_{\mathrm{noise}}(C(\ell)) = \sqrt{\frac{2}{f_{\mathrm{sky}}(2\ell+1)}} \left(C(\ell) + N(\ell)\right). \tag{13}$$

The first term in equation (13) refers to the cosmic variance which describes the fact that we can only observe one realization of the Universe. The second term $N(\ell)$ is the signal expected for an unclustered distribution, which corresponds to shot noise in the case of galaxy distributions, or other sources of noise such as telescope noise in the case of intensity mapping surveys.

The shot noise of the galaxy power spectrum is equal to the solid angle of the survey area divided by the total number of observed galaxies. For the temperature maps, we had to simulate the shot noise by creating a uniform distribution of galaxies in the absence of clustering with the same total galaxy number as the input simulation. We then draw H I masses from the mass distribution of the SKA simulations and converted the galaxy maps into brightness temperature maps. The estimated power spectrum of the temperature noise maps is an estimate of the temperature shot noise of the SKA simulations. This procedure gave the estimate of the shot noise contribution to $N(\ell)$.

We can estimate the receiver noise power spectrum as

$$C_{\mathrm{noise}}(\ell) = \sigma_{\mathrm{rms}}^2 \Omega_{\mathrm{pix}}, \tag{14}$$

where the σ_{rms} is the temperature rms of the unsmoothed map given by equation (2). This theoretical description for the receiver noise gives the second contribution to $N(\ell)$, which we add to the shot noise term.

The beam of an intensity mapping survey is rather wide, in this study we approximated it with a Gaussian beam. We took the most general approach of assuming all the maps are smoothed out to the same angular resolution in the map-making process. We realized this through smoothing the input maps of cosmic signal, beam noise and Galactic foreground to a $\theta_{\mathrm{FWHM}} = 0°\!.3$. The Gaussian beam implies that small scales of the power spectra are suppressed. In order to recover the original power spectrum we divide it by the squared beam window function of a Gaussian beam:

$$W_{\mathrm{beam}}(\ell) = \exp{-\frac{\ell(\ell+1)}{2\ell_{\mathrm{beam}}^2}}, \tag{15}$$

where $\ell_{\mathrm{beam}} = \frac{\sqrt{8\log(2)}}{\theta_{\mathrm{FWHM}}}$.

4.4 Lognormal covariance

As described in Section 3.3, we estimated the covariance matrices in multipole and redshift space with $N_{\mathrm{real}} = 100$ realizations of a lognormal galaxy distribution. The covariance in the measured power spectrum between two multipoles ℓ and ℓ' for one redshift

bin z_i is calculated via

$$\mathrm{Cov}_{z_i}(\ell, \ell') = \frac{1}{N_{\mathrm{real}}-1} \sum_{p=1}^{N_{\mathrm{real}}} (C_{p,z_i}(\ell) - \bar{C}_{z_i}(\ell))(C_{p,z_i}(\ell') \\ - \bar{C}_{z_i}(\ell')), \tag{16}$$

where $C_{p,z_i}(\ell)$ is the power spectrum of the pth realization and $\bar{C}_{z_i}(\ell)$ is the average power spectrum of the N_{real} realizations in one redshift bin z_i. The covariance between identical multipoles at different redshifts is similarly defined as

$$\mathrm{Cov}(z_i, z_j) = \frac{1}{N_{\mathrm{real}}-1} \sum_{p=1}^{N_{\mathrm{real}}} (C_{p,z_i}(\ell) - \bar{C}_{z_i}(\ell))(C_{p,z_j}(\ell) \\ - \bar{C}_{z_j}(\ell)). \tag{17}$$

In the following plots, we show the correlation matrix instead of the covariance matrix, where the diagonal is normalized to one via

$$\mathrm{Cor}_{z_i}(\ell, \ell') = \frac{\mathrm{Cov}_{z_i}(\ell, \ell')}{(\sqrt{\mathrm{Cov}_{z_i}(\ell, \ell)\mathrm{Cov}_{z_i}(\ell', \ell')})}. \tag{18}$$

Figs 3 and 4 give an example of the correlation matrices in multipole for a given redshift bin or in redshift for a given multipole, respectively, showing results both before and after foreground removal. It can be seen in the left-hand panel of Fig. 3 that the correlation between adjacent multipoles is relatively high. The $\mathrm{Cor}(\ell, \ell+1)$ is pictured as the secondary diagonal of the matrix. The other off-diagonal entries are very low as expected for a survey covering sky fraction 0.5. The right-hand side shows the correlation matrix of the power spectra after the foreground removal. It is significantly more contaminated with a complex structure due to correlations introduced by FASTICA.

The sky cut can also introduce correlations between multipoles and to minimize this effect we bin the multipoles. The binned power spectra are weighted according to

$$C(\ell') = \frac{\sum_{\ell=\ell'}^{\ell'+\delta\ell}(2\ell+1)C(\ell)}{\sum_{\ell=\ell'}^{\ell'+\delta\ell}(2\ell+1)}. \tag{19}$$
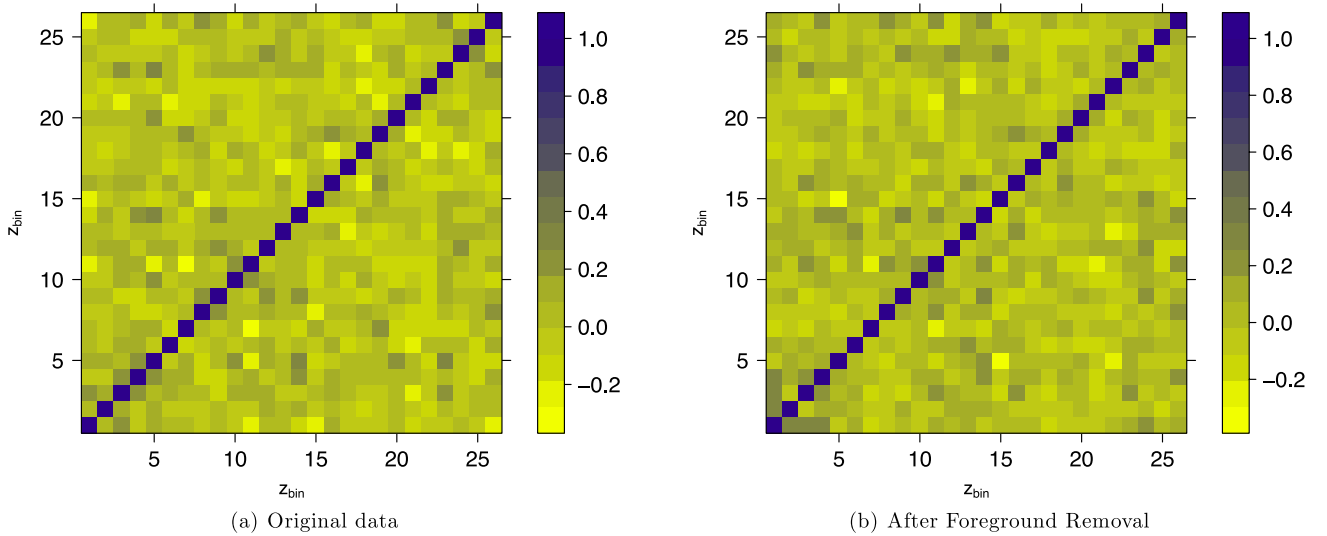
Given that power spectrum measurements at adjacent multipoles exhibit high correlations in Fig. 3, the power spectra are rebinned with $\delta\ell = 2$ for the final analysis. Although the covariance matrix after foreground subtraction has a more complex structure than before, it is acceptable to approximate it as a diagonal form over a wide range of multipoles. The diagonal elements are given in equation (13) where we use the theoretical prediction as $C(\ell)$.

In Fig. 4, the redshift correlations between the bins are shown for one multipole $\ell = 50$. It can be seen in the left-hand panel that the original power spectra have negligible correlations between different redshift slices. After the foreground removal on the right-hand side, the correlations are still very small. This shows that if the cosmological signal has no significant redshift correlations between the bins, the foreground removal will not introduce any.

In this paper, we have not considered the fact that the point spread function (PSF) of the beam will change as a function of frequency. For a frequency-dependent PSF, it is possible that larger correlations as a function of redshift could be found after foreground subtraction as shown in Liu & Tegmark (2011). A possible solution of this effect is to degrade the PSF of all the frequency bands to the largest PSF. This could be done by suitable weighting of the data in the uv plane for interferometric data or as an additional convolution in the map-making process for single-dish experiments. A full simulation of this effect is beyond the scope of this paper and will be left for future work.
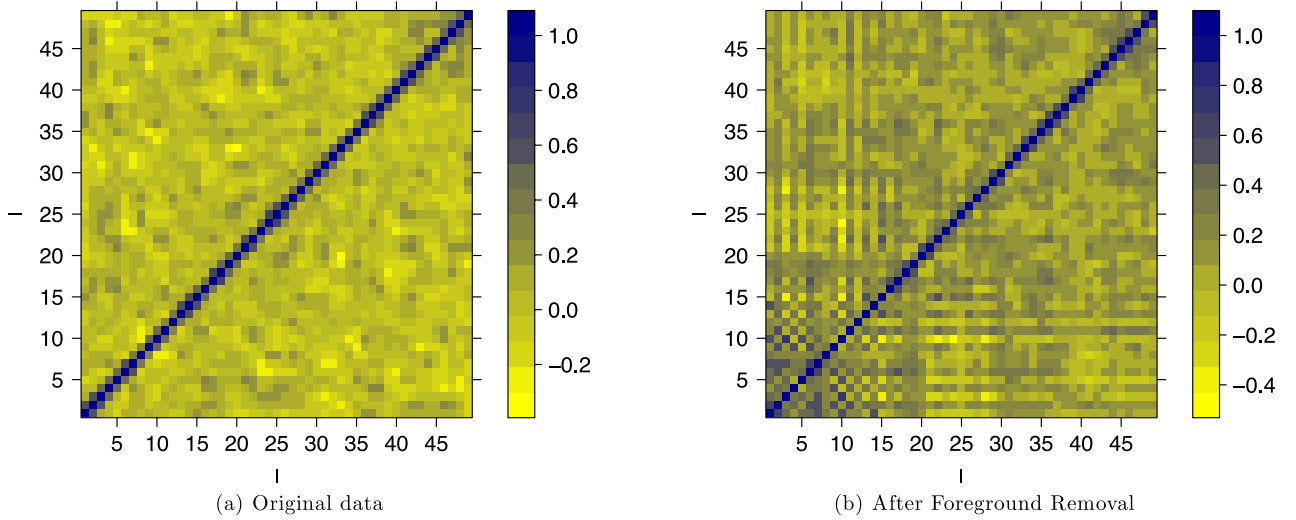
Figure 3. The correlation matrix between power spectrum measurements for the multipole range $1 < \ell < 50$ for an example redshift slice $1.11 < z < 1.16$, computed with the original lognormal realizations in the left-hand panel and including the foreground removal systematics in the right-hand panel. The high values of the elements in the secondary diagonals show the correlation between adjacent multipoles introduced by the sky cut. Additional covariance is introduced by foreground subtraction.

Figure 4. The correlation matrix between power spectrum measurements at different redshifts for an example multipole $\ell = 50$, computed with the original lognormal realizations in the left-hand panel and including the foreground removal systematics in the right-hand panel.

5 FOREGROUND REMOVAL

In this section, the foreground removal technique and its applications to the data are shown. We introduce a masking technique to improve the performance and show the effects on the residuals of the reconstructed cosmological signal.

5.1 FASTICA technique

In the following subsection, the basic principles of the FASTICA method (Hyvärinen 1999) are outlined. For a comprehensive tutorial, we recommend this online tutorial[8] and for scientific applications refer for example to Maino et al. (2002), Bottino, Banday & Maino (2010) and Chapman et al. (2012).

The measurement $\boldsymbol{x}$ is considered to be a linear combination of independent components (ICs) $\boldsymbol{s}$. The basic equation of the ICA is

$$\boldsymbol{x} = \mathbf{A}\boldsymbol{s} = \sum_{i=1}^{N_{\mathrm{IC}}} \boldsymbol{a}_i s_i, \tag{20}$$

where $\mathbf{A}$ is the mixing matrix which contains the weights of the single ICs of which the measured signal is expressed. The columns of the mixing matrix are referred to as $\boldsymbol{a}_i$. The dimensions of $\mathbf{A}$ are (number of measurements) $\times$ (number of ICs). The inverse of equation (20), which is required to determine the unknown ICs of the measurements, is

$$\boldsymbol{s} = \mathbf{W}\boldsymbol{x}, \tag{21}$$

where $\mathbf{W}$ is the weighting matrix which is defined as the inverse of $\mathbf{A}$. A fundamental assumption of this technique is that the ICs have to be statistically independent, which implies that their joint

[8] http://cis.legacy.ics.tkk.fi/aapo/papers/IJCNN99_tutorialweb/

probability density functions (PDFs) is the product of the single PDFs of the variables: $p(y_1, \ldots, y_n) = \prod_{i=0}^{n} p_i(y_i)$. This also implies that the expectation value of the joint functions $f_i(y_i)$ is $E\{f_1(y_1), \ldots, f_n(y_n)\} = \prod_{i=0}^{n} E\{f_i(y_i)\}$. The method cannot determine ICs that are Gaussian distributed since their PDFs are symmetrically distributed and therefore cannot be distinguished.

The approach to identify the unknown ICs s_i and the mixing matrix **A** is based on the central limit theorem. This says that the PDF of a sum of independent variables tends towards a Gaussian distribution. Hence, the PDF of several independent variables is always more Gaussian than that of a single variable. Therefore, the search for one IC is performed by maximizing the non-Gaussianity of an estimated component.

Two possible measures of Gaussianity are the kurtosis and the negentropy. The kurtosis is defined as the normalized fourth moment of a variable: $\mathrm{kurt}(y) = E\{y^4\} - 3E\{y^2\}^2$, which is zero for a Gaussian distributed variable. The negentropy is a slight modification of the entropy: $H(y) = -\int f(y) \log(f(y)) \, dy$. $H(y)$ reaches its maximum for a Gaussian variable since it is the most random and 'disordered' distribution. The negentropy is defined as $J(y) = H(y_{\mathrm{gauss}}) - H(y)$ to set the quantity to zero for a Gaussian variable and make it non-negative. However, the negentropy is computationally hard to determine therefore an approximation of the Non-Gaussianity, which uses the kurtosis, is applied.

5.2 Application

In our application of the FASTICA method, one measurement x_i is a HEALPix map at a given frequency slice with N_{pix} entries of the H I intensity map. Therefore the whole input vector is a matrix of dimension (number of frequencies) × (number of pixels per map). In our analysis, we binned the simulation in $N_{\mathrm{maps}} = 160$ frequency shells and used the HEALPix resolution $N_{\mathrm{pix}} = 12 \times 512^2$ such that we can measure the angular power spectrum to $l_{\mathrm{max}} \simeq 500$. The ICs are hence HEALPix maps of the same resolution. As explained in Section 3.4 the receiver noise is a realization of a Gaussian PDF, therefore, the FASTICA does not consider it to be part of the ICs. The Galactic foregrounds can be up to 5 mag higher than the original cosmological signal. Hence, the method only identifies the Galactic foregrounds as the ICs and the difference between reconstruction and input map is the recovered signal plus the receiver noise. However, the mean temperature T_{mean} of the cosmological signal simulations is a smooth function of redshift and is therefore incorporated into the ICs of the analysis. Therefore, the residual maps require to be renormalized to the T_{mean} of the input maps.

We performed the foreground removal with $N_{\mathrm{IC}} \in \{1, 2, 3, 4, 5, 6\}$ as can be seen in Fig. 5. It is evident that an analysis with less than four ICs does not remove the foregrounds sufficiently, such that they leak into the reconstructed cosmological signal. For the case of four ICs or more, we see that the cosmological data is well recovered for multipoles larger than 50. The Galactic foreground is particularly high in the Galactic plane and therefore contaminates the large-scale structure reconstruction. We chose four ICs to be optimal in our analysis. In the following, we test the effect of different masking in order to reduce the large-scale contamination.

5.3 Masking

The radio emission from the Milky Way is particular high in the Galactic plane in comparison to the emission at higher latitudes. This causes the power spectrum reconstruction to be poorer on
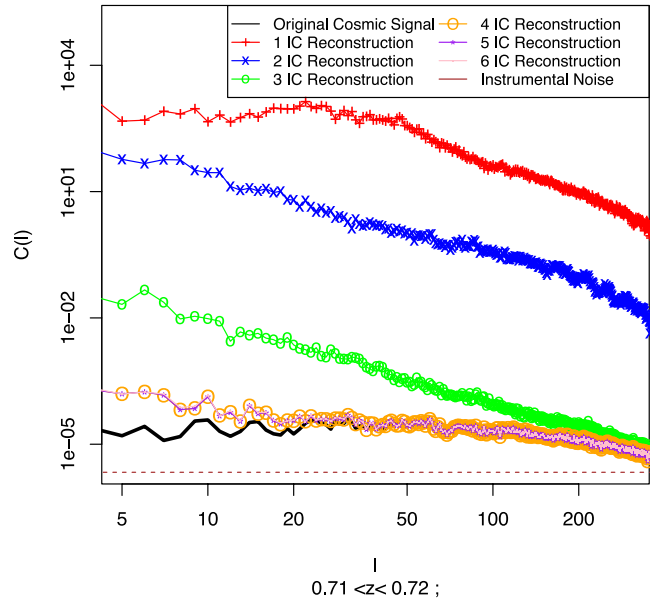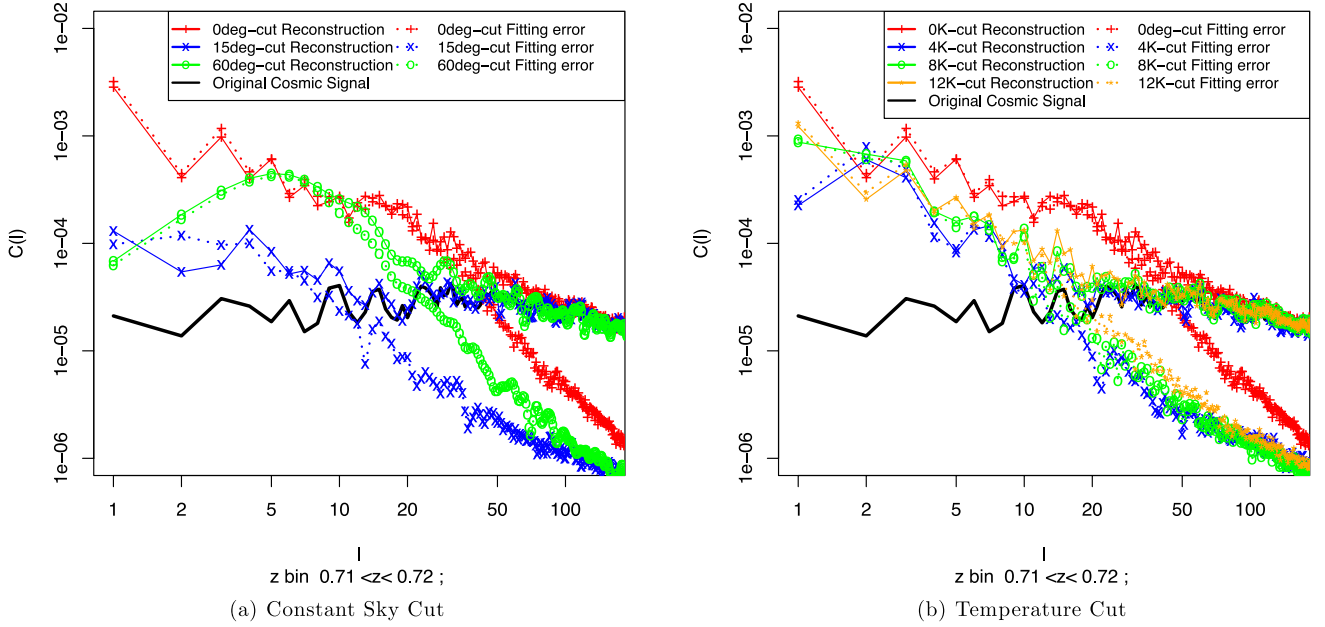

Figure 5. Power spectra of the original cosmological signal (black), the receiver noise (brown), the recovered cosmological signal after the foreground removal (coloured) for number of ICs 1 (red), 2 (yellow), 3 (green), 4 (light blue), 5 (dark blue) and 6 (pink).

large-scales. It is convenient to mask the input data to decrease the contamination. The aim is to strike a balance between including the largest possible survey area and removing the areas of the most dominating foreground emission. We examined the output of FASTICA with unmasked input data, as seen in the previous section. We calculated the fitting error of the temperature, which is the difference between the reconstructed cosmological signal T_{rec} and the input cosmological signal T_{CS} plus noise T_{NO}: $\Delta T_{\mathrm{fit}} = T_{\mathrm{rec}} - T_{\mathrm{CS}} - T_{\mathrm{NO}}$. We considered the power spectrum of the reconstructed cosmological signal in comparison with the power spectrum of the fitting error, and aimed to reduce the latter. For our mask testing, we chose a medium redshift bin of $z = 0.715$.

In creating an optimal mask, we considered two approaches. First, we created a mask with a constant cut in Galactic latitude and applied it to the input data. We examined the cases with a $15°$ and a $60°$ cut. The first case aims to remove the strongest foregrounds in the Galactic plane. The second case, the $60°$ cut, reduces the observed sky area to about $2760 \deg^2$. This simulates a very conservative survey in the North Galactic Pole which is feasible with an SKA pathfinder. We performed the FASTICA on the two cut-sky simulations and find that the masking enhances the quality of reconstruction on larger scales in comparison with an unmasked analysis, as shown in Fig. 6(a). The fitting error decreases in the analysis. However, the constant limit in latitude removes large areas where the foreground temperature is relatively low and hence information on the large scales of the matter distribution is lost.

We circumvented the aforementioned loss of information by creating a mask by applying a threshold T_{max} on the temperature of the Galactic foreground. We mask the pixels above T_{max} and thereby do not lose 'good' pixels with low latitude. In Fig. 6(b) the outcome of applying different foreground thresholds to the data is pictured. The error for the masked FASTICA results is always smaller than for an unmasked experiment. We conclude that an appropriate threshold in our study is $T_{\mathrm{max}} = 8\,\mathrm{K}$, where the fitting error is relatively small while preserving a large sky area. The fitting error is less than the power spectrum signal for $\ell > 20$, which is a great improvement

Figure 6. Power spectra of the original cosmological signal (black), the reconstructed cosmic signal (solid coloured) and the fitting error (dotted coloured) for different masks with no Galactic cut (red) and Galactic cuts of $\theta = 15°$ (green) and $\theta = 60°$ (blue) with four ICs in the left-hand panel. The same original power spectrum (black) is shown in the right-hand panel for different masks with threshold on the foreground temperature $T_{max} = 0$ (red), 4 (green), 8 (light blue) and 12 K (dark blue) with four ICs. This figure shows results for the $0.71 < z < 0.72$ frequency slice.

compared to the case of no masking where systematic errors were dominant for $\ell < 50$.

For the cosmological analysis in Section 6 we consider two cases: the constant latitude cut of $60°$ to mock an SKA precursor experiment and the half-sky simulation masking in foreground temperature above 8 K. The masked Galactic foregrounds for the different cases are shown in Fig. 7.

5.4 Residual projection

To evaluate the performance of the FASTICA, we calculate the amount of Galactic foreground and recovered signal that leak into each other. Each element (foreground, cosmic signal, noise) constituting the input data can be projected on to the reconstructed elements via the mixing matrix. We can therefore split the fitting error into the contributions of the single constituents and deepen our understanding of the sources of the systematic errors.

In the case of the Galactic foreground this is done via the following equation. The residual that leaks into the recovered signal and noise is

$$R_{fg} = fg - (\hat{\mathbf{A}}(\hat{\mathbf{A}}^T\hat{\mathbf{A}})^{-1}\hat{\mathbf{A}}^T)\, fg. \tag{22}$$

In this equation, fg is the input Galactic foreground data from which we subtract the foreground maps projected on to the estimated mixing matrix $\hat{\mathbf{A}}$. Similar to equation (22), we define the noise (no) leakage and the noise plus signal (nocs) leakage as

$$R_{no/nocs} = (\hat{\mathbf{A}}(\hat{\mathbf{A}}^T\hat{\mathbf{A}})^{-1}\hat{\mathbf{A}}^T)(no/nocs). \tag{23}$$

We quantify the leakage maps of the foreground and noise and cosmic signal by calculating their power spectra and comparing these to the original power spectrum of the input simulation. If the foreground leakage is significantly lower than the input power spectra of noise and cosmic signal, the foreground removal worked successfully. Another important goal is that the noise and cosmic
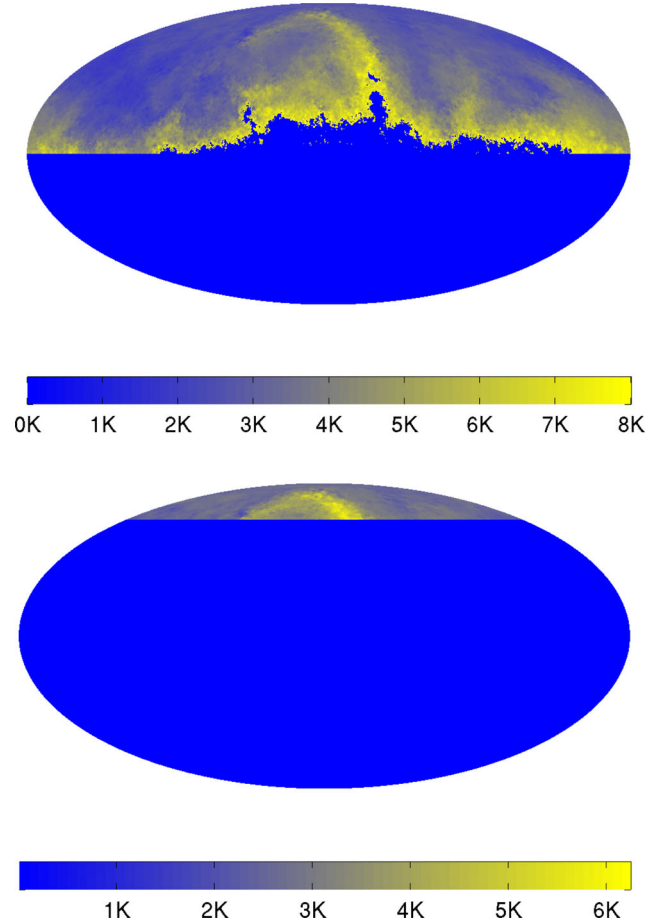
Figure 7. Masked Galactic foreground where pixels with $T > 8$ K are removed in the upper map and with a constant Galactic latitude sky cut of $60°$ in the lower map, shown for the frequency slice $\nu = 829$ MHz.
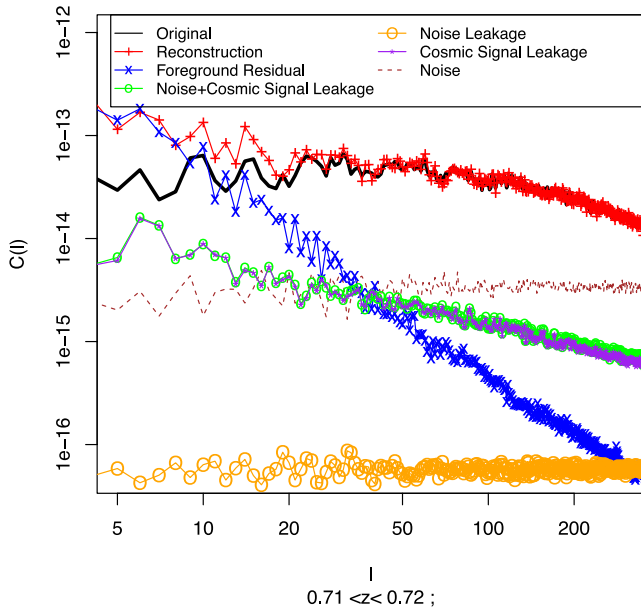
Figure 8. Power spectra of the original cosmological signal (black), the receiver noise (brown), the reconstructed cosmological signal (red), the residuals of the Galactic foreground that leak into the recovered signal (blue), the noise leakage into the foreground reconstruction (yellow), the cosmological signal leakage into the foreground reconstruction (purple), the cosmological signal plus noise leakage into the foreground reconstruction (green) with 8 K cut-off mask and four ICs. Results are for the frequency slice $0.71 < z < 0.72$.

signal leakage is lower than the original power spectrum, otherwise too much of the signal gets lost into the foreground reconstruction.

In Fig. 8, we show the residual leakage for the mask with cut in temperature $T_{max} = 8$ K and four ICs. The variance of the noise and cosmic signal leakage is lower than the original power spectrum on all scales and we can be confident that we recover most of the information of the original signal. The contaminations of the foreground are only significant on small multipoles and become very small for large multipoles. This confirms the previous findings that the large scales are contaminated by residuals of the Galactic foreground.

6 COSMOLOGICAL ANALYSIS

We now consider the cosmological implications of the systematic errors in the power spectrum induced by the foreground subtraction by fitting model power spectra and baryon oscillations in each slice. In these analyses the power spectrum is estimated from rebinned temperature maps with redshift width $\delta z \approx 0.05$. We use $N_{zbin} = 27$ redshift shells within the range $0.01 < z < 1.49$.

6.1 Relative systematic errors

In Section 5, we have shown that the systematic errors compared to the absolute value of the power spectra are relatively small. In the following, we consider the systematics relative to the statistical errors in the power spectrum to understand how relevant they are in the cosmological analysis.

In Fig. 9, the systematic errors in the power spectrum defined as $|C_{sys}(\ell)| = |C_{orig}(\ell) - C_{cleaned}(\ell)|$ are divided by the statistical errors given by equation (13). The relative systematics are given as

a function of redshift on the *x*-axis and multipole on the *y*-axis in a natural logarithmic scale. The errors are binned with $\delta\ell = 20$.

For the first five redshift bins, there are high contaminations on the small scales which show a redshift dependence. This is due to resolution limitations of the large-scale structure simulation since the $10\,\mathrm{Mpc}\,h^{-1}$ cell size subtends an angular scale corresponding to a decreasing multipole value as redshift decreases. Besides the errors caused by the low resolution, the redshift bins on the edges of the data cube cannot be well recovered by the FASTICA due to less line-of-sight information. The large-scale contamination can be seen as the high values in the bottom row of the matrix plots. In addition, the removal leaves contaminations throughout the whole scale range of the power spectrum. The systematic errors on small scales are not very high in power. In addition, they become significant relative to the cosmic variance, which is very small for high ℓ. The mean relative systematic errors in Fig. 9(a) is about 20σ, which is caused by the high errors at the edges of the data cube. The systematics in the black box, however, lie between 0 and 1.3σ with a mean error of 0.5σ. The behaviour of the relative systematics as a function of z and ℓ is very similar for the two different cases of masking. For the $60°$ sky cut in Fig. 9(b), the relative systematics are of smaller power because the statistical error scales with sky area, which is a factor of 6.7 smaller than for the 8 K – temperature cut shown in Fig. 9(a).

In the following cosmological parameter estimation, we consider the relatively uncontaminated power spectrum in the range $20 < \ell < 300$ in the redshift bins 5–26, outlined by the black square in Fig. 9.

6.2 Cosmological parameter estimation

First we estimate the best-fitting cosmological parameters $\boldsymbol{p}$ of the power spectrum. We calculate the $\chi^2(\boldsymbol{p})$ value of the parameters on a grid in parameter space. In the following, the 1σ, 2σ and 3σ contours for $\boldsymbol{p} = (\Omega_m, w_0)$ with different choices of multipole range are presented. We marginalize over the bias parameter b. The remaining cosmological parameters are unchanged and set to the fiducial model described in Section 4.2. As motivated in Section 4.4, we use a diagonal covariance matrix, which results in the following simple form of the $\chi^2(\boldsymbol{p})$:

$$\chi^2(\boldsymbol{p}) = \sum_{i=1}^{N_{zbin}} \sum_{\ell'=\ell_{min}}^{\ell_{max}} \frac{(C_{data,z_i}(\ell) - C_{theory,z_i}(\ell, \boldsymbol{p}))^2}{Cov_{z_i}(\ell, \ell)}. \tag{24}$$

We want to isolate systematics due to the foreground subtraction. For that reason, the data power spectrum used in the cosmological parameter estimation is based on the fiducial theoretical power spectrum, where we add cosmic variance calculated with the log-normal realizations and the systematics of the foreground removal as given in Section 6.1. This reads as

$$C_{data,z_i}(\ell) = C_{theory,z_i}(\ell) + C_{var,z_i}(\ell) + C_{sys,z_i}(\ell), \tag{25}$$

where the cosmic variance is computed via $C_{var,z_i}(\ell) = C_{log,z_i}(\ell) - \bar{C}_{log,z_i}(\ell)$ and the systematics as described in Section 6.1 as $C_{sys,z_i}(\ell) = C_{cleaned,z_i}(\ell) - C_{orig,z_i}(\ell)$.

The choice of ℓ_{min} is an important consideration for the analysis, since the large scales of the cleaned maps show relics of the Galactic foreground as explained in the previous section. If we choose $\ell_{min} < 20$, no useful parameter estimates can be computed since the systematic error on large scales are too dominant. For that reason, in Fig. 10 we present the parameter contours for $\ell_{min} = \{20, 30\}$. The maximum multipole is held constant as $\ell = 300$. As a reference, the

(a) 8K-temperature sky cut

(b) 60 degree sky cut
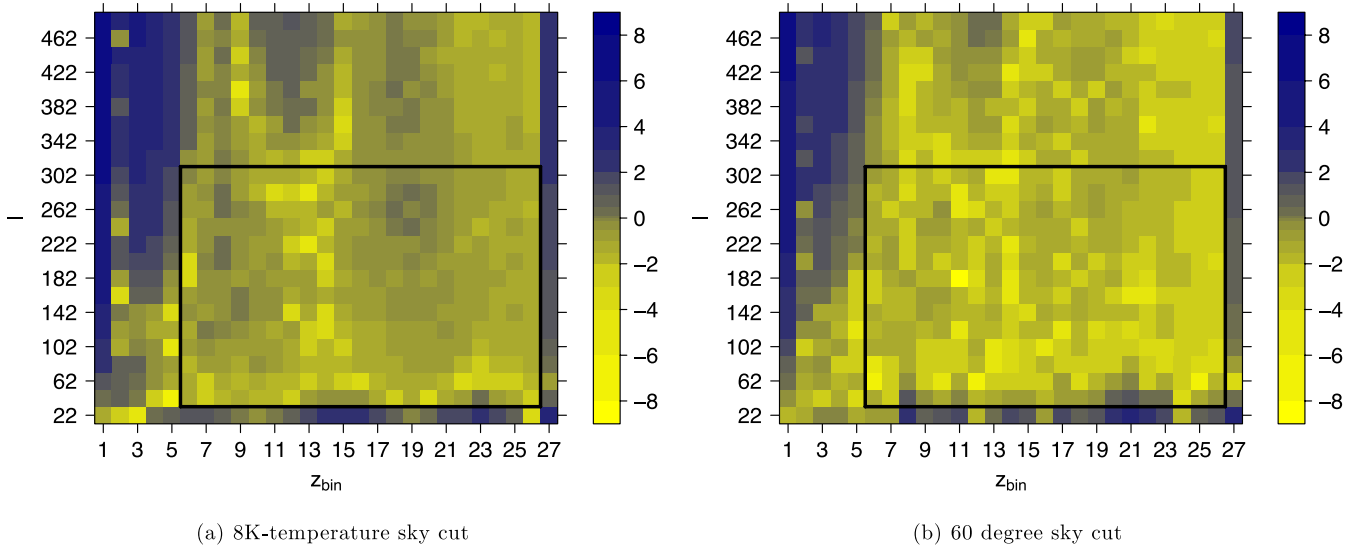
Figure 9. Systematic errors in the power spectrum caused by the foreground subtraction with four ICs divided by the statistical errors described in equation (13) as a function of redshift on the *x*-axis and multipole on the *y*-axis shown in a natural logarithmic scale, hence the relative errors scale between ~3000 and ~3 × 10^{-4}. The relative errors with values greater than 0 imply that the systematic errors are higher than the statistical errors. The right-hand panel shows the analysis of the 8 K temperature cut-sky maps and the left-hand panel the constant cut in latitude with 60°.

parameter contours for an analysis setting $C_{\text{sys}}(\ell) = 0$ are shown with dashed lines where the contours recover the input cosmology marked with a black dot.

In Fig. 10(a), the multipole binning is chosen as $\delta\ell = 2$ due to half-sky coverage of the simulated intensity maps. The green and red solid lines mark the $1\sigma, 2\sigma$ and 3σ parameter constraints which are markedly biased by the foreground removal systematics compared to the dashed lines of the original reference data. However, we note that increasing ℓ_{min} to 30 reduces the parameter bias.

For the 60° cut masking of the intensity maps, the multipoles are more highly correlated due to the small sky cut, hence we use multipole binning $\delta\ell = 10$. This leads to weaker constraints due to the larger cosmic variance error. Apart from higher inaccuracies in Ω_{m} due to the sky cut, the systematic errors induce a similar bias on the contours as in Fig. 10(a). We conclude that the systematics of the foreground removal prevent the recovery of unbiased cosmological parameters.

6.3 Baryon acoustic oscillation fit

We investigate whether the systematic distortions imprinted in the power spectrum shape by foreground removal biased the recovery of cosmic distances by measuring BAO in each redshift slice of the data set using the half-sky masked intensity mapping data. We fitted a BAO model to the angular power spectra both including and excluding the systematic contribution $C_{\text{sys}}(\ell)$ that results from the addition and removal of foregrounds. Our adopted BAO model followed equation (7) in Seo et al. (2012):

$$C_{\text{obs},z_i}(\ell) = B_{z_i}(\ell)C_{\text{theory},z_i}(\ell/\alpha) + A_{z_i}(\ell). \qquad (26)$$

In this equation, $\alpha = D_{\text{A}}(z_i)/D_{\text{A,fid}}(z_i)$ is the fitted scale distortion parameter, applied to the fiducial model angular power spectrum in the *i*th redshift slice $C_{\text{theory},z_i}(\ell)$, which describes the best-fitting angular diameter distance, $D_{\text{A}}(z_i)$, relative to its value in the fiducial cosmology, $D_{\text{A,fid}}(z_i)$. We used the input cosmology of the simulation as the fiducial cosmology, such that $\alpha = 1$ implies that the BAO scale is recovered without bias. We constructed the fiducial angular

power spectrum in each redshift slice, $C_{\text{theory},z_i}(\ell)$, by projecting the input spatial power spectrum of the simulation over the redshift slice. The terms $A_{z_i}(\ell) = \sum_{j=0}^{N_A} A_j \, \ell^j$ and $B_{z_i}(\ell) = \sum_{j=0}^{N_B} B_j \, \ell^j$ are polynomials whose coefficients we marginalize over to describe general power-spectrum shape distortions. We find that a second-order polynomial, $N_A = N_B = 2$, produces a good description of the systematic contribution.

In each redshift slice we binned the angular power spectrum measurements in multipole bands $\delta\ell = 10$. The covariance matrix of the measurements, assumed diagonal given the wide sky area covered ($f_{\text{sky}} = 0.5$) and the tests described above, was constructed using the description in Section 4.4. The covariance matrix of the foreground-subtracted measurements was obtained by adding and removing foregrounds from each realization. We performed the fits by varying the BAO parameter α over a grid for each redshift slice, and for each value of α using a downhill simplex technique to minimize the χ^2 statistic varying the polynomial coefficients A_j and B_j. We fitted the model over the multipole range $50 < \ell < 400$.

The BAO wiggles, produced by dividing the measured power spectrum by a model generated using the 'no-wiggles' power spectrum of Eisenstein & Hu (1998), of an unbiased power spectrum and of the one after foreground removal are plotted in Fig. 11, where it can be seen that the position of the wiggles remains unchanged. Fig. 12 compares the measurements of α from data without any foregrounds, and following the addition and removal of foregrounds. We note that our capacity to extract the BAO signature is not biased by the foreground removal technique.

7 CONCLUSIONS

We have created the most realistic simulation to date of a future half-sky H I intensity mapping experiment that includes H I in galaxies with an appropriate mass function and clustering, Galactic foregrounds with appropriate frequency correlations and receiver noise for a range of different experiments. We apply foreground removal to this map using FASTICA, and reconstruct the cosmological signal. We show that four ICs are the optimal reconstruction choice,
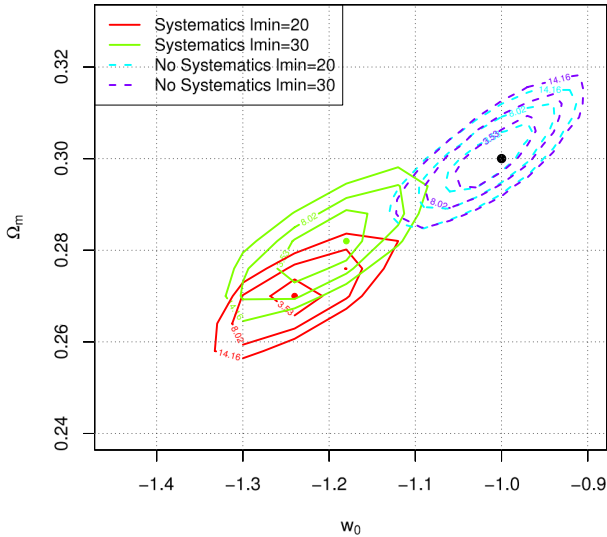
(a) 8K-temperature sky cut
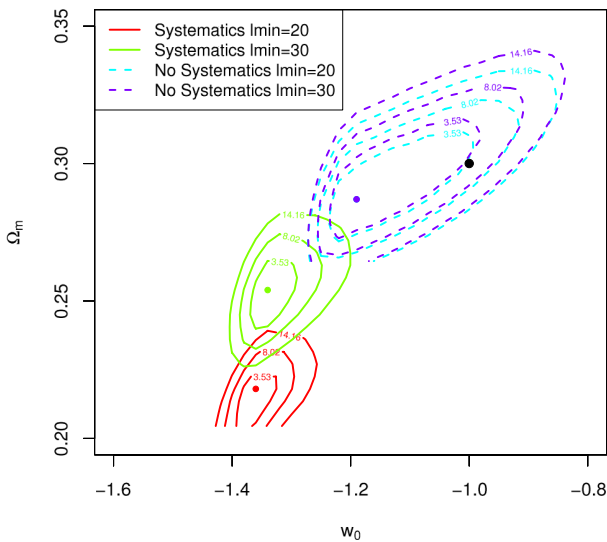
(b) 60 degree sky cut

Figure 10. 1σ, 2σ and 3σ contours of the χ^2 values of Ω_m and w_0 marginalized over galaxy bias, for the uncontaminated power spectrum (dashed lines) and the power spectrum including the systematics of the foreground removal (solid lines) for analysis run with different ℓ_{min}. The black dot shows the fiducial cosmological model. The coloured dots mark the best-fitting values found by the parameter estimation for the different cases. The foreground subtraction biases the recovery of the cosmological parameters.

and consider applying masks based on either Galactic latitude or foreground intensity level. Best results are obtained after masking pixels with brightness temperatures $> 8\,K$. With this method, the reconstructed cosmological power spectra contain scale-dependent systematic errors compared to the input cosmological model which are on average 50 per cent of the statistical error for the multipole range $20 < \ell < 300$ in the redshift bins considered in the analysis. The systematics bias the recovery of cosmological parameters that depend on the overall shape of the power spectrum. These systematic errors are not ameliorated by imposing a stricter Galactic plane or foreground intensity cut. The validity of the presented conclusions is restricted to the analysis with the chosen foreground subtraction method. The systematic errors might reduce and exhibit
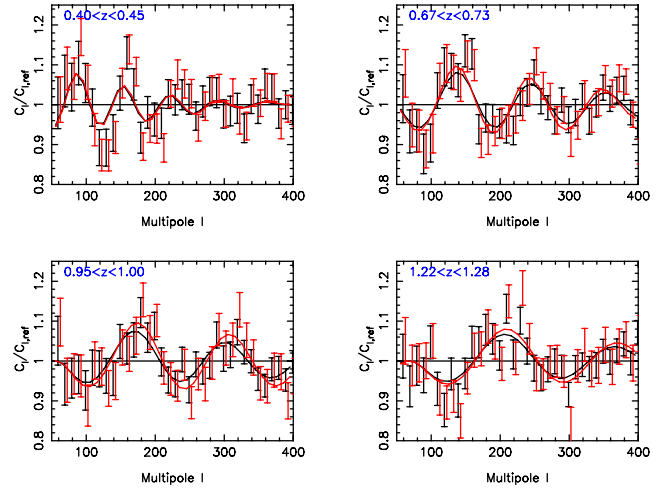
Figure 11. The BAO wiggles shown in example redshift slices. Black and red points show measurements using data without any foregrounds, and following the addition and removal of foregrounds, respectively. The underlying lines give the fitted model to the data points.
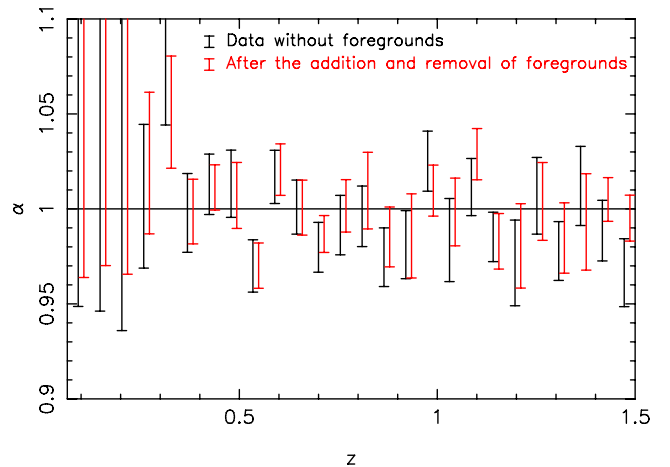
Figure 12. The BAO distortion scale α measured in a series of redshift slices, such that $\alpha = 1$ equates to the input cosmological model. Black and red points show measurements using data without any foregrounds, and following the addition and removal of foregrounds, respectively.

different behaviour on small- and large scales for other subtraction methods.

Furthermore, the addition and removal of foregrounds imprints significant and complex correlations between power spectrum multipoles that are not present in the raw cosmological signal. In order to understand such correlations, future intensity mapping experiments will require a large suite of realistic simulations.

Despite the presence of these systematic errors we show that the signature of BAOs may nonetheless be recovered in an unbiased manner from the intensity mapping survey, using standard techniques that combine a template acoustic-oscillation model with broad-band polynomial shape terms, with free coefficients which are marginalized.

We conclude that, for a range of intensity mapping experiments, FASTICA cannot extract the power spectrum of the cosmological signal in an unbiased manner. However, the BAO signature can nonetheless be obtained in an unbiased way, and we therefore suggest that such surveys will be extremely powerful for mapping

cosmic distances in a redshift range which is difficult for optical surveys to access.

In future work, various foreground removal techniques and their imprints into the recovered cosmological signal should be compared. Furthermore, polarized data and particularly the issue of polarization leakage require investigation in simulated data sets. In addition, we are planning to apply FASTICA to existing intensity maps of the GBT (Switzer et al. 2013).

REFERENCES

Abdalla F. B., Rawlings S., 2005, MNRAS, 360, 27
Abdalla F. B., Blake C., Rawlings S., 2010, MNRAS, 401, 743
Ansari R., Le Goff J., Magneville C., Moniez M., Palanque-Delabrouille N., Rich J., Ruhlmann-Kleider V., Yèche C., 2008, arXiv e-prints (arXiv:0807.3614)
Ansari R. et al., 2012, A&A, 540, A129
Battye R. A., Browne I. W. A., Dickinson C., Heron G., Maffei B., Pourtsidou A., 2013, MNRAS, 434, 1239
Bernardi G. et al., 2010, A&A, 522, A67
Blake C. A., Abdalla F. B., Bridle S. L., Rawlings S., 2004, New Astron. Rev., 48, 1063
Blake C., Collister A., Bridle S., Lahav O., 2007, MNRAS, 374, 1527
Blake C. et al., 2011, MNRAS, 418, 1707
Bottino M., Banday A. J., Maino D., 2010, MNRAS, 402, 207
Carilli C. L., Rawlings S., 2004, New Astron. Rev., 48, 979
Chang T.-C., Pen U.-L., Peterson J. B., McDonald P., 2008, Phys. Rev. Lett., 100, 091303
Chang T.-C., Pen U.-L., Bandura K., Peterson J. B., 2010, Nature, 466, 463
Chapman E. et al., 2012, MNRAS, 423, 2518
Chen X., 2012, Int. J. Modern Phys. Conf. Ser., 12, 256
Condon J., 1992, ARA&A, 30, 575
de Oliveira-Costa A., Tegmark M., Gaensler B. M., Jonas J., Landecker T. L., Reich P., 2008, MNRAS, 388, 247
Dillon J. S., Liu A., Tegmark M., 2013, Phys. Rev., 87, 043005
Di Matteo T., Perna R., Abel T., Rees M. J., 2002, ApJ, 564, 576
Di Matteo T., Ciardi B., Miniati F., 2004, MNRAS, 355, 1053
Doyle M. T. et al., 2005, MNRAS, 361, 34
Efstathiou G., 2004, MNRAS, 348, 885
Eisenstein D. J., Hu W., 1998, ApJ, 496, 605
Gleser L., Nusser A., Benson A. J., 2008, MNRAS, 391, 383
Gong Y., Chen X., Silva M., Cooray A., Santos M. G., 2011, ApJ, 740, L20
Harker G. et al., 2009, MNRAS, 397, 1138

Haslam C., Salter C., Stoffel H., Wilson W., 1982, A&AS, 47, 1
Huterer D., Knox L., Nichol R. C., 2001, ApJ, 555, 547
Hyvärinen A., 1999, IEEE Trans. Neural Networks, 10, 626
Jarvis M. J., Rawlings S., 2004, New Astron. Rev., 48, 1173
Jelic V. et al., 2008, MNRAS, 389, 1319
Lewis A., Challinor A., Lasenby A., 2000, ApJ, 538, 473
Lidz A., Furlanetto S. R., Oh S. P., Aguirre J., Chang T.-C., Doré O., Pritchard J. R., 2011, ApJ, 741, 70
Liu A., Tegmark M., 2011, Phys. Rev., 83, 103006
Liu A., Tegmark M., 2012, MNRAS, 419, 3491
Liu A., Tegmark M., Bowman J., Hewitt J., Zaldarriaga M., 2009, MNRAS, 398, 401
Maino D. et al., 2002, MNRAS, 334, 53
Masui K. W. et al., 2013, ApJ, 763, L20
Mo H., White S. D., 1996, MNRAS, 282, 347
Moore D. F., Aguirre J. E., Parsons A. R., Jacobs D. C., Pober J. C., 2013, ApJ, 769, 154
Morales M. F., Bowman J. D., Hewitt J. N., 2006, ApJ, 648, 767
Oh S. P., Mack K. J., 2003, MNRAS, 346, 871
Peebles P. J. E., 1973, ApJ, 185, 413
Percival W. J. et al., 2001, MNRAS, 327, 1297
Peterson J. B., Suarez E., 2012, arXiv e-prints (arXiv:1206.0143)
Peterson J. B. et al., 2009, Astro2010: The Astronomy and Astrophysics Decadal Survey, Science White Papers, no. 234
Petrovic N., Oh S. P., 2011, MNRAS, 413, 2103
Press W. H., Schechter P., 1974, ApJ, 187, 425
Pritchard J. R., Loeb A., 2012, Rep. Progress Phys., 75, 086901
Pullen A., Dore O., Bock J., 2013, ApJ, submitted (arXiv:1309.2295)
Santos M. G., Cooray A., Knox L., 2005, ApJ, 625, 575
Seo H.-J. et al., 2012, ApJ, 761, 13
Shaw J. R., Sigurdson K., Pen U.-L., Stebbins A., Sitwell M., 2014, ApJ, 781, 57
Sheth R. K., Tormen G., 1999, MNRAS, 308, 119
Sullivan M., Mobasher B., Chan B., Cram L., Ellis R., Treyer M., Hopkins A., 2001, ApJ, 558, 72
Switzer E. R. et al., 2013, MNRAS, 434, L46
Tegmark M., Hamilton A. J., Xu Y.-Z., 2002, MNRAS, 335, 887
Tegmark M. et al., 2004, ApJ, 606, 702
Tegmark M. et al., 2006, Phys. Rev. D, 74, 123507
Testori J. C., Reich P., Bava J. A., Colomb F. R., Hurrel E. E., Larrarte J. J., Reich W., Sanz A. J., 2001, A&A, 368, 1123
Thomas S. A., Abdalla F. B., Lahav O., 2011, Phys. Rev. Lett., 106, 241301
Thompson A. R., Moran J. M., Swenson G. W., Jr, 2004, Interferometry and Synthesis in Radio Astronomy. Wiley-VCH Verlag GmbH, Weinheim
van Haarlem M. et al., 2013, A&A, 556, A2
Visbal E., Trac H., Loeb A., 2011, J. Cosmol. Astropart. Phys., 1108, 010
Vujanovic G., Staveley-Smith L., Pen U.-L., Chang T.-C., Peterson J., 2009, ATNF Proposal C2098, Semester: July 2009, p. 2491
Wang X.-M., Tegmark M., Santos M., Knox L., 2006, ApJ, 650, 529
Willott C. J., Rawlings S., Blundell K. M., Lacy M., Eales S. A., 2001, MNRAS, 322, 536
Wilman R. et al., 2008, MNRAS, 388, 1335
Wyithe S., Loeb A., Geil P., 2008, MNRAS, 383, 1195
Yun M. S., Reddy N. A., Condon J. J., 2001, ApJ, 554, 803
Zwaan M. A. et al., 2003, AJ, 125, 2842

This paper has been typeset from a TEX/LATEX file prepared by the author.